LA-UR-20-30420
Approved for public release; distribution is unlimited.

Title: Ab Initio Phase Diagram of Tungsten

Author(s): Burakovsky, Leonid
Baty, Samuel R.
Preston, Dean Laverne

Intended for: Report

Issued: 2020-12-22

Ab Initio Phase Diagram of Tungsten

S.R. Baty[1], L. Burakovsky[2], and D.L. Preston[3]

[1] *Analytics Intelligence and Technology,*

[2] *Theoretical Division,*

[3] *Computational Physics Division,*

Los Alamos National Laboratory,

Los Alamos, New Mexico 87545, USA

Abstract

The phase diagram of tungsten (W) to a pressure (P) of 2500 GPa is investigated using a comprehensive *ab initio* approach that includes (i) the calculation of the zero temperature (T) free energies (enthalpies) of different solid structures, (ii) the quantum molecular dynamics simulation of the melting curves of different solid structures, (iii) the derivation of the analytic form for the solid-solid phase transition boundary, and (iv) the simulations of the solidification of liquid W into the final solid states on both sides of the solid-solid phase transition boundary, in order to confirm the corresponding analytic form. There are two solid structures confirmed to be present on the phase diagram of W, the ambient body-centered cubic (bcc) and the high-pressure double hexagonal close-packed (dhcp). At $T = 0$, the bcc-dhcp transition occurs at 1060 GPa, and the transition boundary has a positive slope dT/dP : the bcc-dhcp-liquid triple point is at $(P, T) =$ (1675 GPa, 23680 K).

PACS numbers: 64.10.+h, 64.70.Dv, 64.70.Kb, 71.15.Pd, 81.30.-t, 81.30.Bx

INTRODUCTION

Body-centered cubic (bcc) transition metals such as vanadium (V), niobium (Nb), molybdenum (Mo) and tungsten (W) are technologically important materials. The mechanical behavior of these metals under high static pressures has been a subject of interest since the pioneering work of Bridgman [1]. The advantages of W such as, e.g., the high strength and thermal conductivity, the low thermal expansion, low tritium inventory and low erosion rate, make it attractive to be used in a wide range of applications for future fusion power plants [2, 3]. Refractory metals such as W and its alloys are also finding increasing structural applications which involve impact loading [4], and the high density (19.3 g/cm^3), high strength, good ductility, and high melting point makes tungsten an attractive candidate material. The mechanical properties of the material at high pressures (P) and/or high temperatures (T), as well as high strain rates is of great importance in the design and analysis of such applications. Unfortunately, W has been one of the less studied materials, so that its phase diagram, specifically the high-P melting curve and a possible high-P–high-T (HP-HT) polymorphism which its materials strength modeling crucially depends on, has remained virtually unknown.

Research interest in HP-HT polymorphism in the bcc transition metals has reemerged in connection with laser-heated diamond anvil cell (DAC) melting experiments in which melting curves with a small slope (dT/dP) in the megabar pressure range have been determined [5–12]. These flat melting curves do not agree with the results of more recent experiments [13–19] and calculations [20–25]. Several hypotheses have been proposed to explain these apparent discrepancies. One of them suggests that the flat melting curves could in fact correspond to solid-solid (s-s) phase boundaries that occur under HP-HT below melting. In particular, HP-HT solid-solid transitions have been predicted to take place in Ta [24, 26, 27] and Mo [28]. In contrast to these metals, there are only few studies on (W). The experimental melting curve of W is one of the flat ones [7]; it has a slope of $\sim 7-8$ K/GPa and reaches ~ 4000 K at ~ 100 GPa which contradicts both the initial slope of 44 K/GPa from isobaric expansion measurements [29] and the shock Hugoniot melting points of ~ 12000 K at ~ 400 GPa [30]. The experimental melting curves of Refs. [31], [32] and [33] have even higher slopes of ~ 90, 75 and 60 K/GPa, respectively. As noted in [33], large experimental errors of Ref. [34] lead to $\sim 50\%$ error in the value

of the corresponding slope, 70 ± 35 K/GPa. The other, theoretical, value of the slope is 28.7 K/GPa [35].

Here we present an extensive theoretical study of the phase diagram of W to a pressure of 2500 GPa (25 Mbar).

THE PHASE DIAGRAM OF W

Although the phase diagram of W has not been known in detail, there are several features of this phase diagram that have been firmly established. First, melting on the shock Hugoniot of W occurs at ~ 400 GPa and presumably at $T \sim 12000$ K [30]; these values are extracted from the corresponding $P = P(U_p)$ and $T = T(U_p)$ dependences on the particle velocity U_p as those at $U_p \sim 2.5$ km/s at which melting occurs on the shock Hugoniot of W [30]. Second, the stability of bcc-W has been confirmed experimentally under room-T isothermal compression to 420 GPa [36] and to 500 GPa [37]. There is presently no experimental evidence for a s-s transition in W. However, there is compelling theoretical evidence for a s-s phase transition at high P. Calculations of the phonon spectra of both the bcc and face-centered cubic (fcc) structures of W show that bcc-W becomes mechanically unstable at pressures above 12 Mbar, while fcc-W being mechanically unstable at low P gets fully stabilized above 4 Mbar [38]. A very recent theoretical study [39] demonstrates that fcc-W becomes mechanically stable at ~ 450 GPa while bcc-W becomes mechanically unstable with increasing P; above 12 Mbar bcc-W is unstable at low T but remains stable above 1000 K. Hence, a s-s phase transformation to another solid phase that is mechanically stable is expected to occur at $P \lesssim 12$ Mbar at low T, and the s-s transition boundary is expected to have positive slope ($dT/dP > 0$) since the bcc-W stability range widens with increasing T. Because fcc-W also becomes thermodynamically more stable than bcc-W [39], fcc-W is one of the candidates for the high-P solid structure of W. In fact, the bcc-fcc s-s phase transition was predictied to occur at ~ 12 Mbar, and calculations show that the bcc-fcc phase boundary does have positive slope at $P \geq 12$ Mbar [39]. However, in [40] a transformation to a different solid structure, namely, dhcp, which is thermodynamically more stable than fcc, is predicted to occur, albeit at much lower pressure of 650 GPa. If a bcc-dhcp s-s phase transition does occur in W, just like in Mo [41], the two phase diagrams may look similar. As we

demonstrate in what follows, this is indeed the case.

We begin our theoretical study of the phase diagram of W with the calculation of the cold ($T = 0$) free energies (i.e., enthalpies) of a number of different solid structures of W as a function of P.

Cold enthalpies of different solid structures of W

The calculations were based on density-functional theory (DFT) with the projector-augmented-wave (PAW) [42] implementation and the generalized gradient approximation (GGA) for exchange-correlation energy, in the form known as Perdew-Burke-Ernzerhof (PBE) [43]. All the calculations were done using VASP (Vienna Ab initio Simulation Package). Since the simulations were performed at high-PT conditions, we used accurate pseudopotentials where the semi-core 5s and 5p states were treated as valence states. Specifically, W was modeled with 14 valence electrons per atom (5s, 5p, 5d, and 6s orbitals). Cold enthalpies were calcualted using unit cells with very dense k-point meshes (e.g., $50 \times 50 \times 50$ for bcc-Nb) for high accuracy. In all the non-cubic cases we first relaxed the structure to determine its unit cell parameters at each volume.

Our calculated cold enthalpies of five different solid structures of W are shown in Fig. 1. It is seen that, with inceasing P, a number of other solid structures become thermodynamically more stable than bcc, but it is dhcp that does it first, at a pressure of 1060 GPa. Hence, in the case of W the s-s transition boundary is the bcc-dhcp one, and its starting point is $(P, T) = (1060, 0)$.

Equations of state of bcc-W and dhcp-W

Next, we calculate the cold equations of state of both bcc-W and dhcp-W. For dhcp-W, we also determine the density dependence of the c/a ratio, where a and c are the lattice constants of the dhcp unit cell.

Our *ab initio* results on the cold equation of state (EOS) of bcc-W are described by the third-order Birch-Murnaghan (BM3) form

$$P(\rho) = \frac{3}{2} B_0 \left(\left(\frac{\rho}{\rho_0} \right)^{7/3} - \left(\frac{\rho}{\rho_0} \right)^{5/3} \right) \left[1 + \frac{3}{4} (B_0' - 4) \left(\left(\frac{\rho}{\rho_0} \right)^{2/3} - 1 \right) \right], \qquad (1)$$

where B_0 and B_0' are the values of the bulk modulus and its pressure derivative at the reference point $\rho = \rho_0$. In our case of bcc-W,

$$\rho_0 = 19.3 \text{ g/cm}^3, \quad B_0 = 314.1 \text{ GPa}, \quad B_0' = 4.07. \tag{2}$$

Since the $P = 0$ values of the density of W at $T = 0$ and 300 K differ by $\sim 0.3\%$ (19.31 vs. 19.26 g/cc), and $T = 300$ K introduces a negligibly small thermal pressure correction, the $T = 0$ and $T = 300$ K isotherms can be described by the same values of B_0 and B_0'. Consequently, we can compare room-T isotherm data of Refs. [37, 44–47] to our $T = 0$ isotherm as determined from QMD. A comparison is shown in Fig. 2. It is seen that our EOS is virtually identical to the experimental isotherm of [47], for which $B_0 = 317.5$ GPa and $B_0' = 4.05$ are very similar to ours, as well as to the theoretical calculations of [45] in the so-called mean-field potential (MFP) approach.

For dhcp-W, the P dependence of the c/a ratio for the lattice constants of the dhcp unit cell is accurately described by

$$\frac{c}{a} \;=\; 3.2660 \;-\; 0.4912 \left(\frac{a}{a_0}\right)^3 \;+\; 0.7484 \left(\frac{a}{a_0}\right)^5, \tag{3}$$

where $a_0 = 2.8525$ Å coresponds to the ideal ($c/a = 4\sqrt{2/3} \approx 3.2660$) unit cell of the same reference density ρ_0 as for the corresponding cold EOS. Since the unit cell volume is $ca^2\sqrt{3}/8$ ($a^3/\sqrt{2}$ for the ideal structure), the above relation can be translated into the P dependence of c/a, via the corresponding cold EOS of dhcp-W that we obtained. It is described by the BM3 form, Eq. (1), with

$$\rho_0 = 18.6 \text{ g/cm}^3, \quad B_0 = 290.8 \text{ GPa}, \quad B_0' = 3.95. \tag{4}$$

Above 1000 GPa, the dhcp-W structure is virtually ideal. At the transition pressure of 1060 GPa, the two density values predicted by these EOSs are, respectively (in g/cm^3), 40.38 for bcc-W and and 40.53 for dhcp-W; hence the bcc-dhcp transition corresponds to a small volume change of $\sim 0.4\%$.

MELTING CURVES OF DIFFERENT SOLID STRUCTURES OF W

We now discuss the calculation of the melting curves of different solid structures of W. For this calculation, we used the Z method which is described in detail in [24, 48, 49]. We

calculated the melting curves of bcc-W as well as a number of other solid structures of W which have been mentioned in the literature in connection with transition metals: all the close-packed structures with different layer stacking (fcc, hcp, dhcp, thcp, 9R), open structures (simple cubic, A15, hex-ω), and different orthorhombic structures. Again, in all the non-cubic cases we relaxed the structure to determine its unit cell parameters; those unit cells were used for the construction of the corresponding supercells. We used systems of 400-500 atoms in each case.

Ab initio **melting curve of bcc-W**

For the calculation of the melting curve of bcc-W (with the Z method) we used a 432-atom ($6 \times 6 \times 6$) supercell with a single Γ-point. Full energy convergence (to $\lesssim$ 1 meV/atom) was verified by performing short runs with $2 \times 2 \times 2$ and $3 \times 3 \times 3$ k-point meshes and comparing their output with that of the run with a single Γ-point. For each of the five points listed in Table 1, we performed ten NVE runs (five values of V correspond to five values of densities in Table 1) of 10000-20000 time steps of 1 fs each, with an increment of the initial T of 250 K for the first datapoint, 750 K for the last datapoint, and 625 K for the remaining four. Since the error in T is half of the increment [49], the T errors of our six values of T_m are within 5% each. The P errors are negligibly small: less than 1 GPa for the first point and 1-2 GPa for the remaining five. Hence, our melting results on bcc-W are very accurate.

lattice constant (Å)	density (g/cm^3)	P_m (GPa)	T_m (K)	ΔT_m (K)
3.350	16.240	-17.7	2800	125.0
3.050	21.519	90.6	6520	312.5
2.850	26.375	258	9840	312.5
2.675	31.897	543	13760	312.5
2.535	37.479	947	18070	312.5
2.400	44.166	1596	23130	375.0

Table 1. The six *ab initio* melting points of bcc-W, (P_m, $T_m \pm \Delta T_m$), obtained from the

Z method implemented with VASP.

The best fit to the six bcc-W melting points gives the melting curve of bcc-W in the Simon-Glatzel form [50] (T_m in K, P in GPa):

$$T_m(P) = 3695 \left(1 + \frac{P}{41.8}\right)^{0.50}. \quad (5)$$

Its initial slope, $dT_m(P)/dP = 44.2$ K/GPa at $P = 0$, is in excellent agreement with 44 K/GPa from isobaric expansion measurements [29]. Both the five bcc-W melting points and the melting curve (8) are shown in Fig. 3 and compared to experiment [30, 33], the calculated Hugoniot of W [51], and other theoretical calculations [52–55].

Ab initio **melting curve of dhcp-W**

The five melting points of dhcp-W that we obtained are listed in Table 2. The dhcp-W melting simulations were carried out exactly the same way as the bcc ones, namely, 10 runs per point, 10000-20000 time steps of 1 fs each per run, and an increment of the initial T of 300 K for the first datapoint, 750 K for the last datapoint, and 625 K for the remaining four. Just as for bcc-W, a 432-atom ($6 \times 6 \times 3$) supercell was used to simulate each of the six dhcp-W melting points. And as for bcc-W, the T errors of our six values of T_m are within 5% each.

lattice constant (Å)	density (g/cm^3)	P_m (GPa)	T_m (K)	ΔT_m (K)
2.90	17.702	8.1	3080	150.0
2.65	23.199	150	7380	312.5
2.40	31.230	510	13110	312.5
2.25	37.902	970	18000	312.5
2.15	43.440	1471	22200	312.5
2.05	50.112	2235	27380	375.0

Table 2. The six *ab initio* melting points of dhcp-W, (P_m, $T_m \pm \Delta T_m$), obtained from the Z method implemented with VASP. The lattice constant values correspond to the ideal

dhcp structure.

The best fit to the six dhcp-W points gives the melting curve of dhcp-W in the Simon-Glatzel form (T_m in K, P in GPa):

$$T_m(P) = 2640 \left(1 + \frac{P}{23.0}\right)^{0.51}. \tag{6}$$

Figs. 4 and 5 demonstrate the time evolution of T and P, respectively, in the Z-method runs of the bcc-W melting point (P in GPa, T in K) $(P, T) = (947, 18070)$. Figs. 6 and 7 demonstrate the same for the dhcp-W melting point $(970, 18000)$. These two points are chosen as examples and are shown in Fig. 8 as open blue and green circles, respectively.

All the other solid structures that we considered melt below bcc. As two examples, one of the fcc-W melting points, namely, $(P, T) = (942, 16920)$, and one of the 9R-W melting points, namely, $(P, T) = (968, 16390)$, along with short segments of the corresponding melting curves, are shown in Fig. 8. The corresponding time evolution of T and P in the Z-method runs are shown in Figs. 9 and 10, and 11 and 12, respectively.

The melting curves of bcc-W and dhcp-W cross each other at (P in GPa, T in K) $(P, T) = (1675, 23680)$ which is the bcc-dhcp-liquid triple point. The choice of $T(P) = a(1660 - P)^b,\ 0 < b < 1$ as a functional form for the bcc-dhcp phase boundary leads to

(iii) the bcc-dhcp solid-solid phase transition boundary:

$$T(P) \,=\, 73.2\,(P \,-\, 1060)^{\,0.90}; \tag{7}$$

which crosses the triple point and lies within the bounds imposed by the solidification simulations using the inverse Z method. We discuss these inverse Z simulations in the following section.

Although the rigorous derivation of the thermal equations of state of bcc-W and dhcp-W goes beyond the scope of this work, we note that the finite-T counterparts of the above two EOSs can be written approximately as $P(\rho, T) = P(\rho) + \alpha\, T$, where $\alpha_{\rm bcc} = 7.3 \cdot 10^{-3}$ and $\alpha_{\rm dhcp} = 6.8 \cdot 10^{-3}$. The resulting "approximate" thermal EOSs turn out to be quite accurate. For example, for the five bcc-W melting points in Table 1, the corresponding thermal EOS gives pressures of -17.8, 90.3, 258, 543, 948 and 1601, which are basically identical to those in the third column of Table 1. For the five dhcp-W melting points in

Table 2, the five P values are 7.9, 150, 509, 970, 1476 and 2242, in excellent agreement with those in the third column of Table 2.

INVERSE-Z SOLIDIFICATION SIMULATIONS OF LIQUID W

To constrain the location of the bcc-dhcp solid-solid phase boundary on the P-T plane between the points ($P = 1060, T = 0$) and ($P = 1675, T = 23680$), we carried out two sets of independent inverse Z runs [24] to solidify liquid W and to confirm that liquid W solidifies into bcc on one side of this boundary and into dhcp (or any other solid structure) on the other side, such that the location of this phase boundary may be constrained. We used a computational cell of 512 atoms prepared by melting a $8 \times 8 \times 8$ solid simple cubic (sc) supercell which would eliminate any bias towards solidification into bcc or any other solid structure (fcc, hcp, dhcp, etc.). We used sc unit cells of 2.0, 1.935, 1.915, 1.895, and 1.870 Å; the dimensions of bcc unit cells having the same volume as the sc ones are 2.520, 2.438, 2.413, 2.388, and 2.356 Å, respectively, which corresponds to the bcc-W pressures of $\sim$ 870, 1225, 1355, 1505, and 1715 GPa, and slightly lower pressures for dhcp-W.

We carried out NVT simulations using the Nosé-Hoover thermostat with a timestep of 1 fs, with the initial T increment of 2500 K. Complete solidification typically required from 15 to 25 ps, or 15000-25000 timesteps. The inverse Z runs indicate that liquid W only solidifies into bcc at $\sim$ 900 GPa in the whole temperature range from 0 to essentially the corresponding T_m. However, at $\sim$ 1200-1400 GPa it solidifies into bcc above the transition boundary in Fig. 8, while below this boundary it solidifies into another solid structure. The radial distribution functions (RDFs) of the final solid states are noisy; upon fast quenching of the seven structures (seven green bullets in Fig. 8 in the 1200-1400 GPa range) to low T, where RDFs are more discriminating, and by comparing them to the RDFs of fcc, hcp, dhcp, 9R, etc., we conclude that dhcp is the closest strucure to those that liquid W solidies into below the transition boundary.

The RDFs of the solidified states at $\sim$ 1200 GPa above the transition boundary are shown in Fig. 13, and of those solidified below the transition boundary in Fig. 14. The 7500 K state virtually lies on the boundary. We tentatively assign it to bcc, because it definitely has features of bcc (RDF peaks at $R \sim 55$, 65 and 85, etc.). At the same time it certainly has some features that are both uncharacteristic of bcc (e.g., the disappearance

of the bcc peak at $R \sim 95$) and characteristic of dhcp (peaks at $R \sim 90$ and 120, small peaks at $R \sim 100$ and 130, etc.). Most likely, this 7500 K state is bcc with some admixture of dhcp.

A few more comments are in order. The 17500 K state at ~ 1250 GPa did not solidify, most likely for the reason of not being supercooled enough to intiate the solidification process [24]. Indeed, 17500 K constitutes ~ 0.8 of the corresponding T_m of ~ 22000 K (20% of supercooling) while, e.g., for the other set of points at ~ 900 GPa, the highest solidification T of 12500 K constitutes ~ 0.75 of the corresponding T_m of ~ 17000 K (25% of supercooling) which apparently allows for the solidification process to go through in this case.

The phase diagram of W to 2500 GPa is shown in Fig. 8. It includes the two, bcc and dhcp, melting curves, the bcc-dhcp solid-solid phase transition boundary, and the results of the solidification of liquid W into final states of either solid bcc or solid dhcp, using the inverse Z method.

The W phase diagram figure does not show the previous experimental DAC melting curve of Errandonea *et al.* [7, 56] which is flat, with a slope of $\sim$ 7-8 K/GPa. We did not include it in Fig. 8 because we do not consider it to be relevant to our study. The very recent experimental study by Hrubiak *et al.* [17] demonstrates that, on increasing T, compressed Mo undergoes a transformation that results in a texture (microstructure) change: large Mo grains become unstable at high T due to high atom mobility and reorganize into smaller crystalline grains. This transformation occurs below melting, and the pressure dependence of the transformation temperature is consistent with the previous DAC melting curve by Errandonea *et al.* [7]. Hence, most likely, Errandonea's curve is an intermediate DAC transition boundary rather than the true melting curve of Mo. The latter has the initial slope of 34 K/GPa, and both its most recent experimental measurements [17] and theoretical calculations [41, 57] agree with each other.

A behavior similar to that of Mo (a texture change) was recently observed in the high-PT melting experiments on V [19]. Hence, this phenomenon of a texture (microstructure) change can be common to a number of transition metals, including W. It is therefore natural to assume that in the case of W, too, the corresponding Errandonea's melting curve is an intermediate DAC transition boundary, while our curve is the actual melting curve of W.

CONCLUDING REMARKS

The phase diagrams of substances can be topologically similar (look-alike) or, in some cases, even topologically equivalent. The topological similarity of the phase diagrams of Ti, Zr, and Hf (each containing the three solid phases α, β and ω) is well known. The phase diagrams of Si and Ge are topologically equivalent at low P : both contain semiconducting diamond and metallic tetragonal β-Sn solid structures, and the slopes of the corresponding solid-solid and solid-liquid phase boundaries are almost identical [59]; in either case, $dT_m/dP(0) < 0$. The proper knowledge of similarities of the phase diagrams can be useful in making predictions with regard to the phase diagram content and in offering suggestions as to what solid structures to look for in high-PT experiments.

The results of the present study demonstrate that the phase diagrams of W and Mo, Group 6B partners in the periodic table, shown in Fig. 8 of this article and Fig. 11 of Ref. [41], respectively, are similar. In both cases, the ambient bcc solid structure transforms into dhcp on increasing P. Only these two solid phases are confirmed as being present on the two phase diagrams, via *ab initio* QMD simulations using the Z methodology.

It is interesting to note another case of the phase diagrams of Nb and Ta, Group 5B partners in the periodic table, which appear to be similar as well. In both cases, a bcc-Pnma solid-solid phase transition occurs [24, 58] but, in contrast to dhcp in Mo and W, the orthorhombic Pnma phase exists at high T only. In Ta, the bcc-Pnma-liquid triple point is at a pressure which is an order of magnitude higher than that in Nb [24, 58]. Also, the bcc-Pnma transition T increases with P in Nb but decreases with T in Ta.

Fast recrystallization observed in HP-HT experiments on transition metals may imply either a microstructural transition (discussed above) at which the sample texture changes but its crystal structure remains the same, or a true solid-solid phase transition. The former was recently proven to be the case in Mo [17], and it is very likely the case in V [19] as well as in W. The latter is apparently the case in Nb [58] and likely in Re as well [25]. In either case, the corresponding fast recrystallization lines have been misinterpreted as flat melting curves in the former laser-heating DAC experiments.

Acknowledgments

The work was done under the auspices of the US DOE/NNSA. The QMD simulations were performed on the LANL clusters Pinto and Badger as parts of the Institutional Computing projects w18_meltshear and w19_thermoelast.

[1] P.W. Bridgman, Phys. Rev. **48**, 825 (1935), Rev. Mod. Phys. **17**, 3 (1945), **18**, 1 (1946)

[2] M. Rieth *et al.,* J. Nucl. Mater. **432**, 482 (2013)

[3] R.A. Pitts *et al.,* J. Nucl. Mater. **438**, 48 (2013)

[4] T.W. Penrice, *Metals Handbook,* 9th edition (Metals Park, Ohio, 1984), Vol. 7, p. 688; V. Srikanth and G. Upadhayaya, Refrac. Hard Metals **5**, 49 (1986); L.S. Magness, Mech. Mater. **17**, 147 (1994)

[5] Lazor, P., Shen, G. & Saxena, S.K. Laser-heated diamond anvil cell experiments at high pressure: melting curve of nickel up to 700 kbar. Phys. Chem. Minerals **20**, 86 (1993)

[6] Kavner, A. & Jeanloz, R. High-pressure melting curve of platinum. J. App. Phys. **83**, 7553 (1998).

[7] Errandonea, D.; Schwager, B.; Ditz R.; Gessmann, C.; Boehler, R.; Ross, M. Systematics of transition-metal melting. Phys. Rev. B **63**, 132104 (2001).

[8] Errandonea, D. *et al.* Melting of tantalum at high pressure determined by angle dispersive x-ray diffraction in a double-sided laser-heated diamond-anvil cell. J. Phys. Cond. Mat. **15**, 7635 (2003).

[9] Boehler, R., Santamaría-Perez, D., Errandonea, D. & Mezouar, M. Melting, density, and anisotropy of iron at core conditions: new x-ray measurements to 150 GPa. J. Phys. Conf. Ser. **121**, 022018 (2008).

[10] Santamaría-Perez, D. *et al.* X-ray diffraction measurements of Mo melting to 119 GPa and the high pressure phase diagram. J. Chem. Phys. **130**, 124509 (2009).

[11] Ruiz-Fuertes, J., Karandikar, A., Boehler R. & Errandonea, D. Microscopic evidence of a flat melting curve of tantalum. Phys. Earth Planet. Inter. **181**, 69 (2010).

[12] Yang, L., Karandikar, A. & Boehler, R. Flash heating in the diamond cell: Melting curve of rhenium. Rev. Sci. Instr. **83**, 063905 (2012).

[13] Dewaele, A., Mezouar, M., Guignot, N. & Loubeyre, P. High melting points of tantalum in a laser-heated diamond anvil cell. Phys. Rev. Lett. **104**, 255701 (2010).

[14] D. Errandonea. High-pressure melting curves of the transition metals Cu, Ni, Pd, and Pt. Phys, Rev. B **87**, 054108 (2013).

[15] Anzellini, S. *et al.* Melting of iron at Earth's inner core boundary based on fast X-ray diffraction. Science **340**, 464 (2013).

[16] Lord, O.T. *et al.* The melting curve of Ni to 1 Mbar. Earth Planet. Sci. Lett. **408**, 226 (2014).

[17] Hrubiak, R.; Meng, Y.; Shen, G. Microstructures define melting of molybdenum at high pressures. *Nat. Commun.* **2017**, *8*, 14562.

[18] Anzellini, S. *et al. In situ* characterization of the high pressure – high temperature melting curve of platinum. Sci. Rep. **9**, 13034 (2019).

[19] Errandonea, D. *et al.* Melting curve and phase diagram of vanadium under high-pressure and high-temperature conditions. Phys. Rev. B **100**, 094111 (2019).

[20] Liu, Z-L., Cai, L-C., Chen, X-R. & Jing, F-Q. Molecular dynamics simulations of the melting curve of tantalum under pressure. Phys. Rev. B **77**, 024103 (2008).

[21] Haskins, J., Moriarty, J.A. & Hood, R.Q. Polymorphism and melt in high-pressure tantalum. Phys. Rev. B **86**, 224104 (2012).

[22] Liu, C-M. *et al.* Melting curves and entropy of fusion of body-centered cubic tungsten under pressure. J. Appl. Phys. **112**, 013518 (2012).

[23] Pozzo, M. & Alfe, D. Melting curve of face-centered-cubic nickel from first-principles calculations. Phys. Rev. B **88**, 024111 (2013).

[24] Burakovsky, L., Chen, S.P., Preston, D.L. & Sheppard, D.G. Z methodology for phase diagram studies: platinum and tantalum as examples. J. Phys. Conf. Ser. **500**, 162001 (2014).

[25] Burakovsky, L., Burakovsky, N., Preston, D. & Simak, S.I. Systematics of the third row transition metal melting: the hcp metals rhenium and osmium. Crystals **2018**, 8, 243.

[26] Burakovsky, L. *et al.* High-pressure–high-temperature polymorphism in Ta: resolving an ongoing experimental controversy. Phys. Rev. Lett. **104**, 255702 (2010).

[27] Hu, J. *et al.* Sound velocity measurements of tantalum under shock compression in the 10-110 GPa range. J. Appl. Phys. **111**, 033511 (2012).

[28] Belonoshko, A.B. *et al.* Molybdenum at high pressure and temperature: melting from another solid phase. Phys. Rev. Lett. **100**, 135701 (2008).

[29] Shaner, J.W., Gathers, G.R. & Minichino, C. A new apparatus for thermophysical measurements above 2500 K, High Temp.-High Pres. **8**, 425 (1976).

[30] Hixson, R.S.; Fritz, J.N. Shock compression of tungsten and molybdenum. *J. Appl. Phys.* **1992**, *7*1, 1721.

[31] Musella, M., Ronchi, C. & Sheindlin, M. Dependence of the melting temperature on pressure up to 2000 bar in uranium dioxide, tungsten, and graphite. Int. J. Thermophys. **20**, 1177 (1999).

[32] Kloss, A., Hess. H., Schneidenbach, H. & Grossjohann, R. Scanning the melting curve of tungsten by a submicrosecond wire-explosion experiment. Int. J. Thermophys. **20**, 1199 (1999).

[33] Gustafson, P. Evaluation of the thermodynamic properties of tungsten. Int. J. Thermophys. **6**, 395 (1985).

[34] Vereshchagin, L.F. & Fateeva, N.S. Melting curves of graphite, tungsten and platinum to 60 kbar. Sov. Phys. JETP **28**, 597 (1969).

[35] Gorecki, T. Vacancies and melting curve of metals at high pressure. Z. Metallk. **68**, 231 (1977); Vacancies and a generalised melting curve of metals. High Temp.-High Pres. **11**, 683 (1979).

[36] Ruoff, A.L.; Xia, H.; Xia, Q. The effect of a tapered aperture on x-ray diffraction from a sample with a pressure gradient: Studies on three samples with a maximum pressure of 560 GPa. Rev. Sci. Instrum. **63**, 4342 (1992).

[37] Dubrovinsky, L., Dubrovinskaia, N., Bykova, E., Bykov, M., Prakapenka, V., Prescher, C., Glazyrin, K., Liermann, H.-P., Hanfland, M., Ekholm, M. *et al.* The most incompressible metal osmium at static pressures above 750 gigapascals. Nature **525**, 226 (2015).

[38] Einarsdotter, K., Sadigh, B., Grimvall, G. & Ozoliņš, V. Phonon instabilities in fcc and bcc tungsten. Phys. Rev. Lett. **79**, 2073 (1997).

[39] Zhang, H.-Y.; Niu, Z.-W.; Cai, L.-C.; Chen, X.-R.; Xi, F. *Ab initio* dynamical stability of tungsten at high pressures and high temperatures. Comput. Mater. Sci. **144**, 32 (2018).

[40] Ruoff. A.L., Rodriguez, C.O. & Christensen, N.E. Elastic moduli of tungsten to 15 Mbar, phase transition at 6.5 Mbar, and rheology to 6 Mbar. Phys. Rev. B **58**, 2998 (1998).

[41] Burakovsky, L., Lushcer, D.J., Preston, D., Sjue, S. & Vaughan, D. Generalization of the unified analytic melt-shear model to multi-phase materials: molybdenum as an example.

Crystals **2019**, 9, 86.

[42] Blöchl, P. Projector augmented-wave method. Phys. Rev. B **50**, 17953 (1994).

[43] Perdew, J.P., Burke, K. & and Ernzerhof, M. Generalized gradient approximation made simple. Phys. Rev. Lett. **77**, 3865 (1996).

[44] A.L. Ruoff, H. Xia, H. Luo and Y.K. Vohra, Rev. Sci. Instr. **61**, 3830 (1990)

[45] Y. Wang, D. Chen and X. Zhang, Phys. Rev. Lett. **84**, 3220 (2000)

[46] A. Dewaele, P. Loubeyre and M. Mezouar, Phys. Rev. B **70**, 094112 (2004)

[47] T. Mashimo *et al.,* J. Appl. Phys. **119**, 035904 (2016)

[48] Belonoshko, A.B., Skorodumova, N.V., Rosengren, A. & Johansson, B. Melting and critical superheating. Phys. Rev. B **73**, 012201 (2006).

[49] Burakovsky, L.; Burakovsky, N.; Preston, D.L. *Ab initio* melting curve of osmium. Phys. Rev. B **92**, 174105 (2015).

[50] Simon, F. & Glatzel, G. Bemerkungen zur Schmelzdruckkurve. Z. Anorg. Allgem. Chemie **178**, 309 (1929).

[51] McQueen, R.G. & Marsh, S.P. Equation of state for nineteen metallic elements from shock-wave measurements to two megabars. J. Appl. Phys. **31**, 1253 (1960).

[52] F. Xi and L. Cai, Physica B **403**, 2065 (2008).

[53] J.H. Carpenter, M.P. Desjarlais, A.E. Mattsson and K.R. Cochrane, "A New Wide-Range Equation of State for Tungsten," SNL Report SAND2008-1415C.

[54] C.-M. Liu *et al.*, J. Appl. Phys. **112**, 013518 (2012).

[55] C.-M. Liu *et al.*, Chinese J. Phys. **55**, 2468 (2017).

[56] Santamaría-Pérez, D.; Ross, M.; Errandonea, D.; Mukherjee, G.D.; Mezouar M.; Boehler, R. X-ray diffraction measurements of Mo melting to 119 GPa and the high pressure phase diagram. J. Chem. Phys. **130**, 124509 (2009).

[57] Cazorla, C., Gillan, M.J., Taioli, S. & Alfè, D. Melting curve and Hugoniot of molybdenum up to 400 GPa by *ab initio* simulations. J. Phys. Conf. Ser. **121**, 012009 (2008).

[58] Errandonea, D.; Burakovsky, L.; Preston, D.L.; MacLeod, S.G.; Santamaría-Perez, D.; Chen, S.P.; Cynn, H.; Simak. S.I.; McMahon, M.L.; Proctor, J.E.; Experimental and theoretical confirmation of an orthorhombic phase transition in niobium at high pressure and temperature. Nature Comms. Mat. **1**, 60 (2020).

[59] Burakovsky, L.; Preston, D.L. Defect Diffus. Forum **43**, 210 (2002).

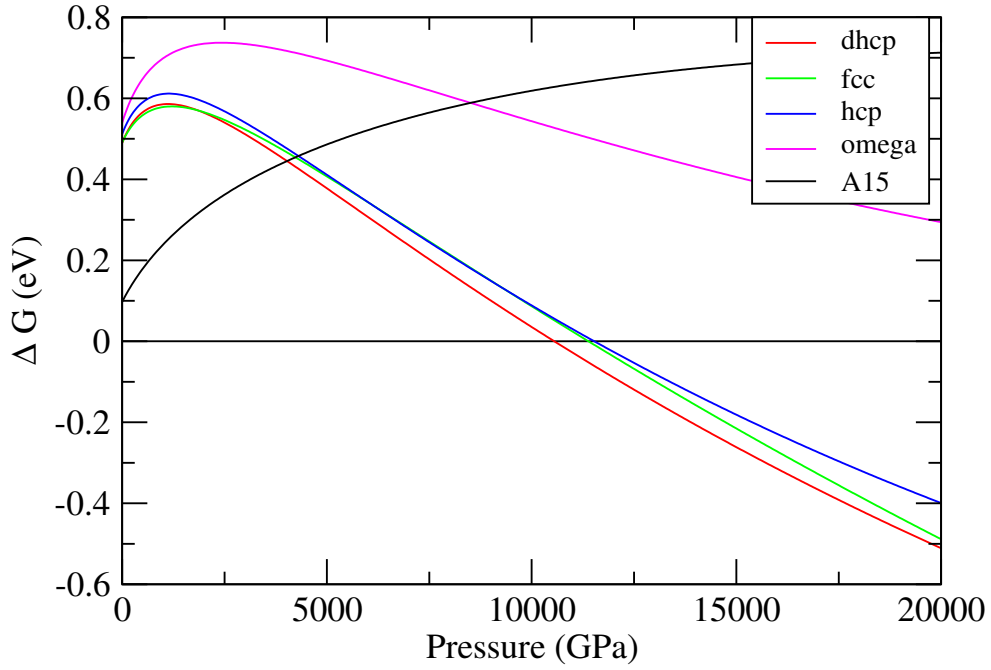

FIG. 1: The $T = 0$ free energies of different solid structures of W (listed in the legend) from *ab initio* calculations using VASP. The free energy of bcc-W is taken to be identically zero.

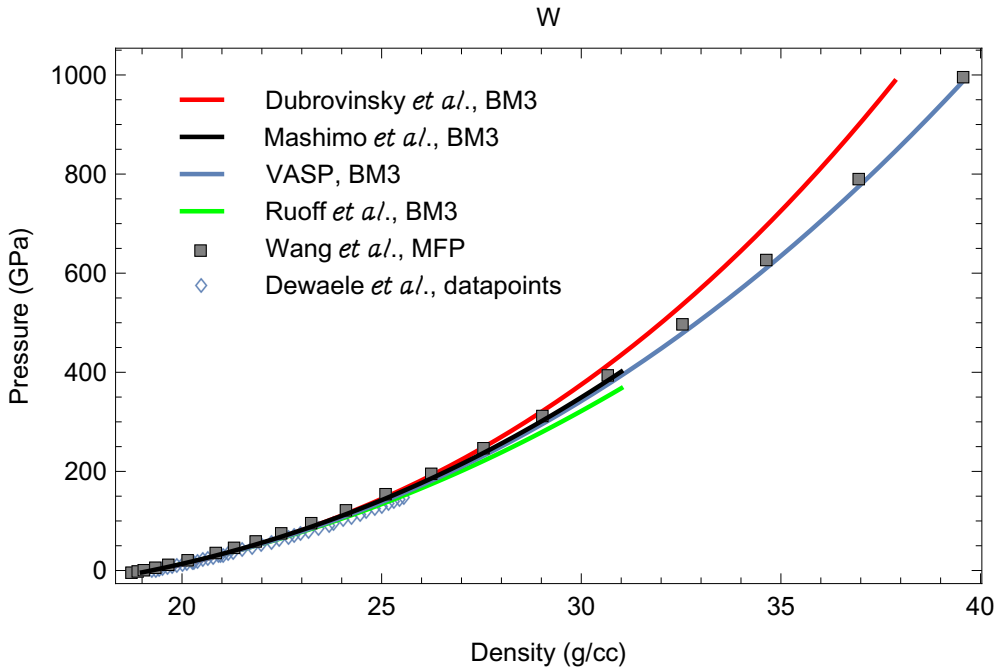

FIG. 2: The $T = 0$ equation of state of bcc-W: our own *ab initio* calculations using VASP vs. experimental [37, 44, 46, 47] and other theoretical [45] data.

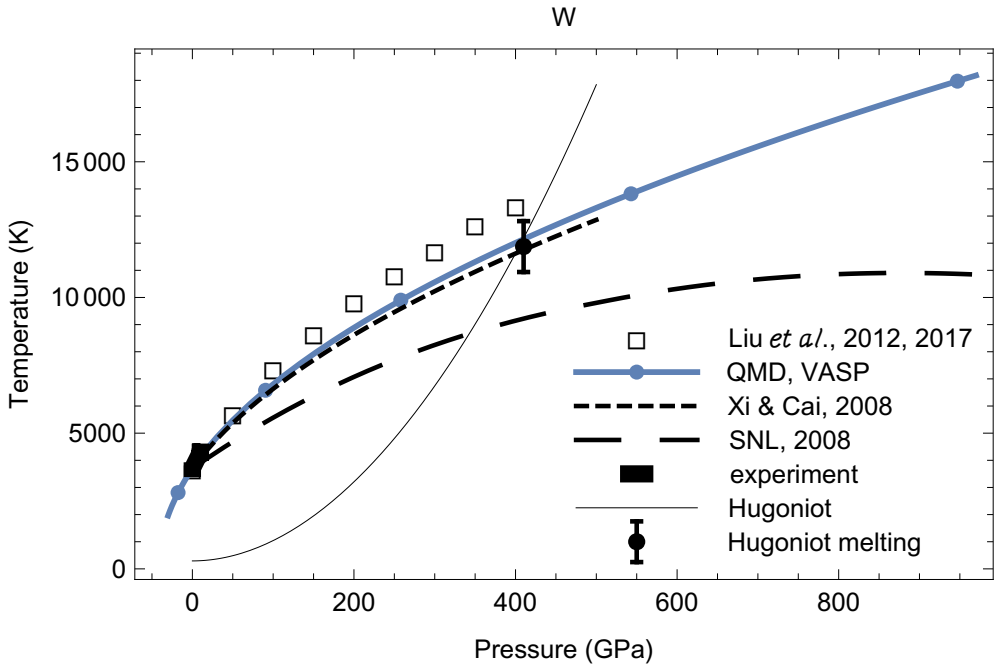

FIG. 3: The melting curve of bcc-W: QMD simulations using VASP vs. other theoretical calculations [52–55], the low-pressure melting data of Ref. [33], and the experimental shock melting datapoint [30]. The calculated Hugoniot is shown as a thin black curve.

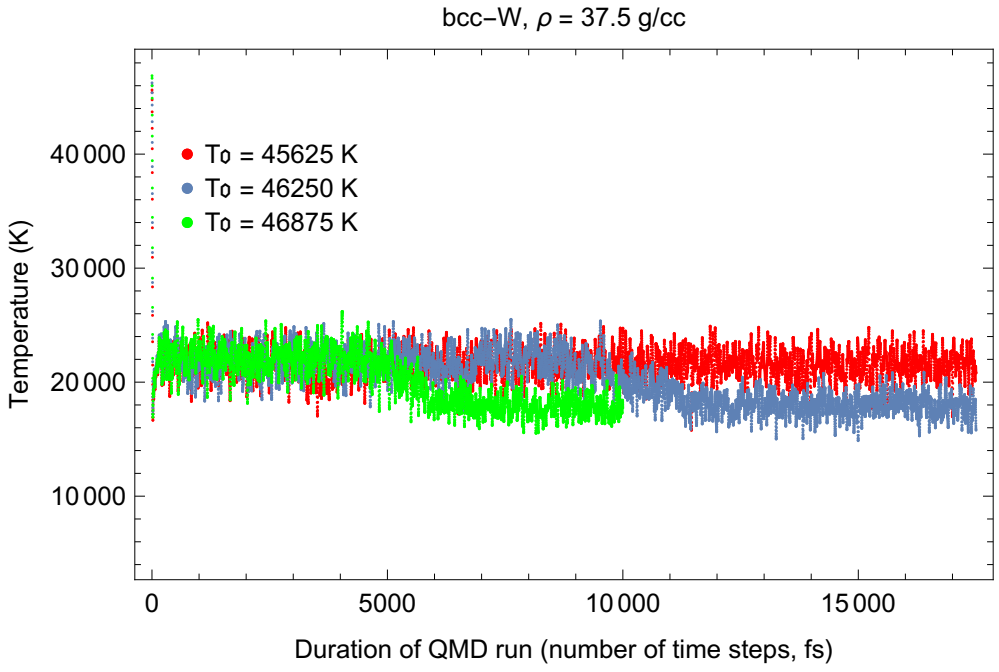

FIG. 4: Time evolution of temperature for bcc-W in three QMD runs with initial temperatures (T_0s) separated by 625 K. The middle run is the melting run, during which T decreases from $\sim$ 22000 K for the superheated state to $\sim$ 18000 K for the liquid at the corresponding melting point.

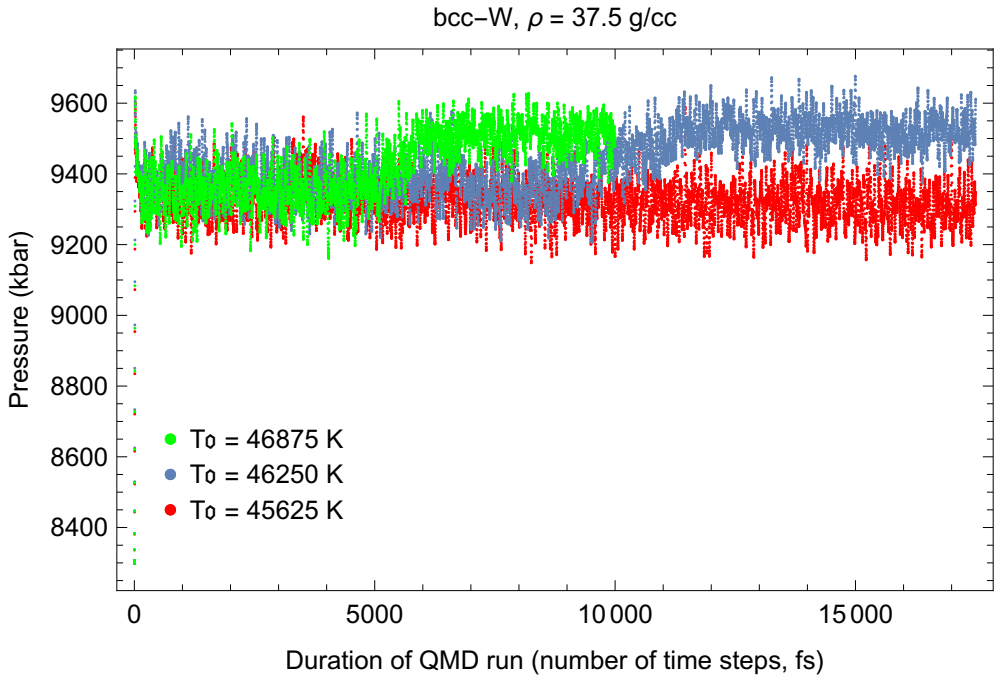

FIG. 5: The same as in Fig. 4 for the time evolution of pressure (in kbar; 10 kbar = 1 GPa). During melting P increases from $\sim$ 930 GPa for the superheated state to $\sim$ 950 GPa for the liquid at the corresponding melting point.

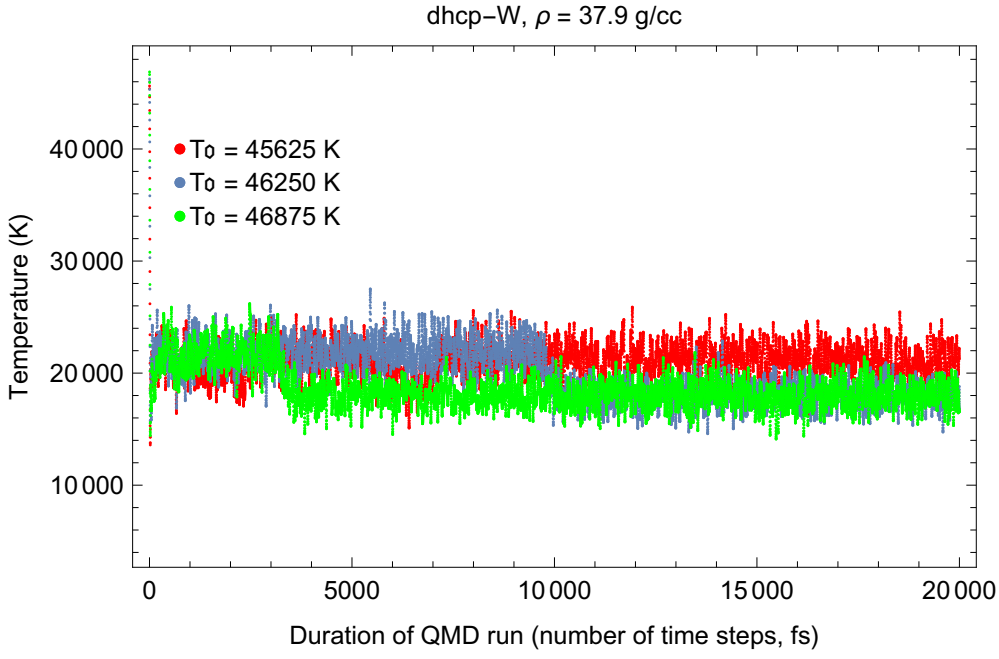

FIG. 6: The same as in Fig. 4 for dhcp-W.

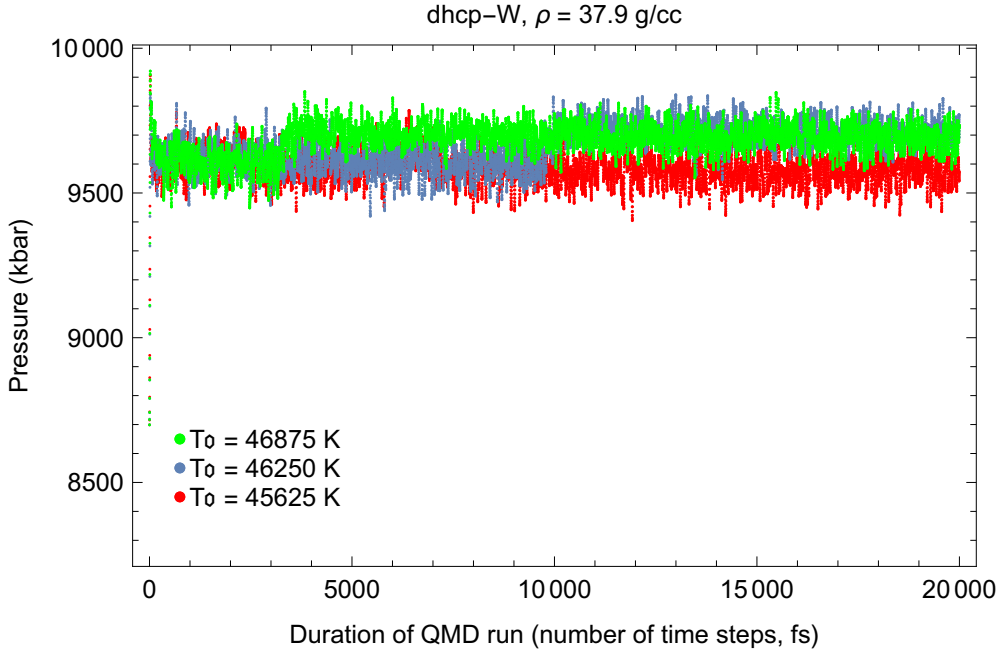

FIG. 7: The same as in Fig. 5 for dhcp-W.

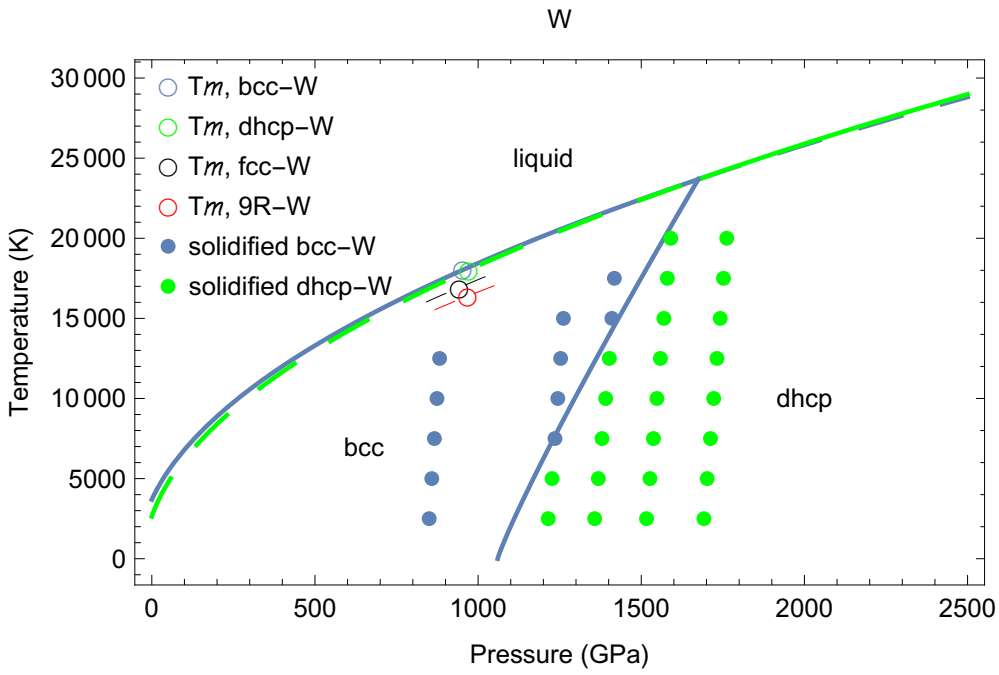

FIG. 8: *Ab initio* phase diagram of tungsten.

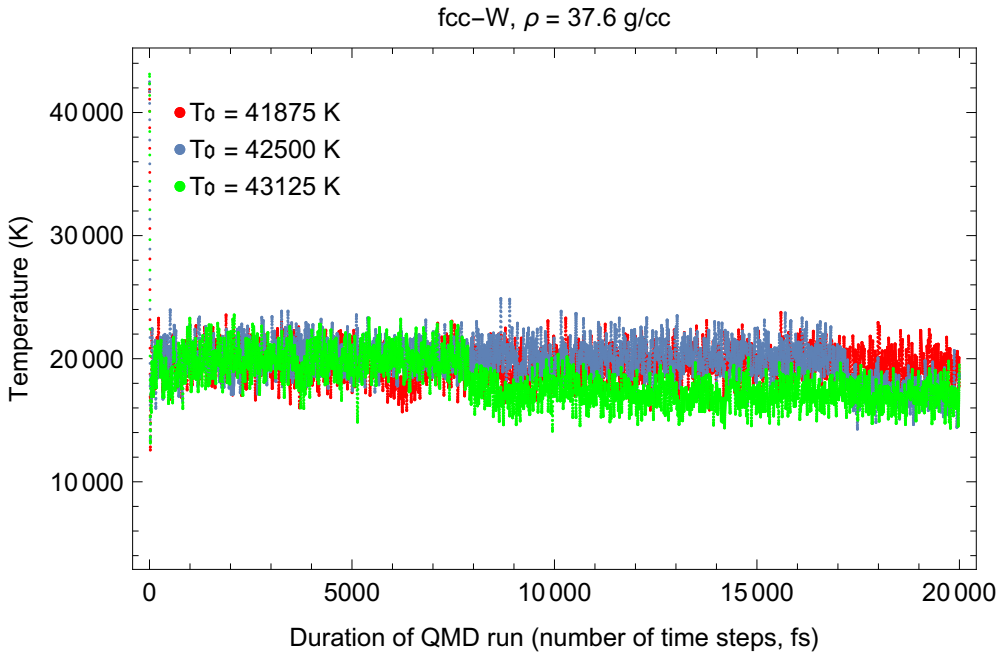

FIG. 9: The same as in Fig. 4 for fcc-W.

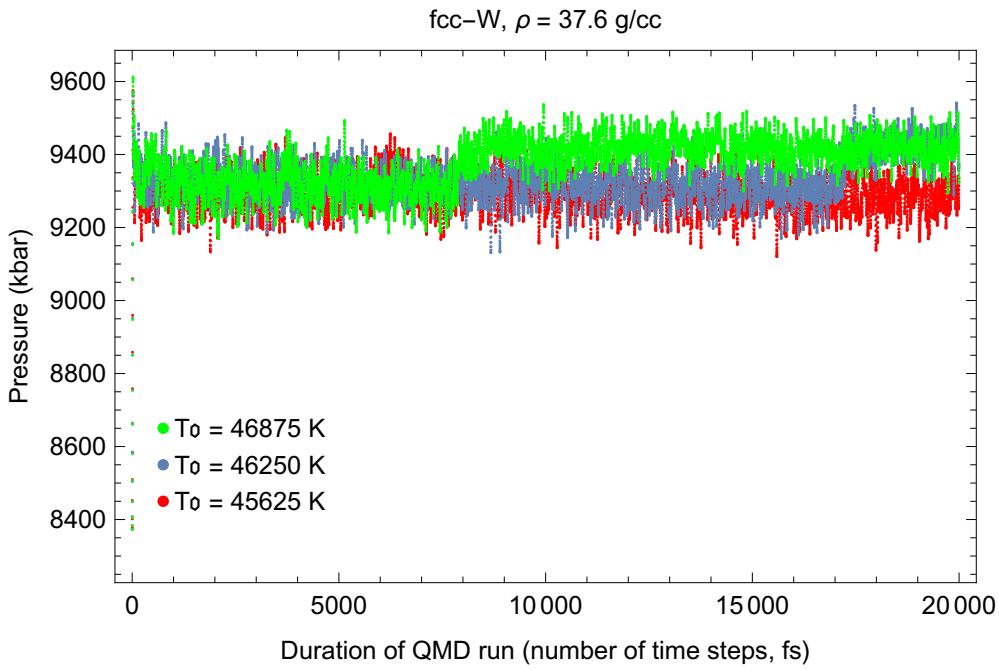

FIG. 10: The same as in Fig. 5 for fcc-W.

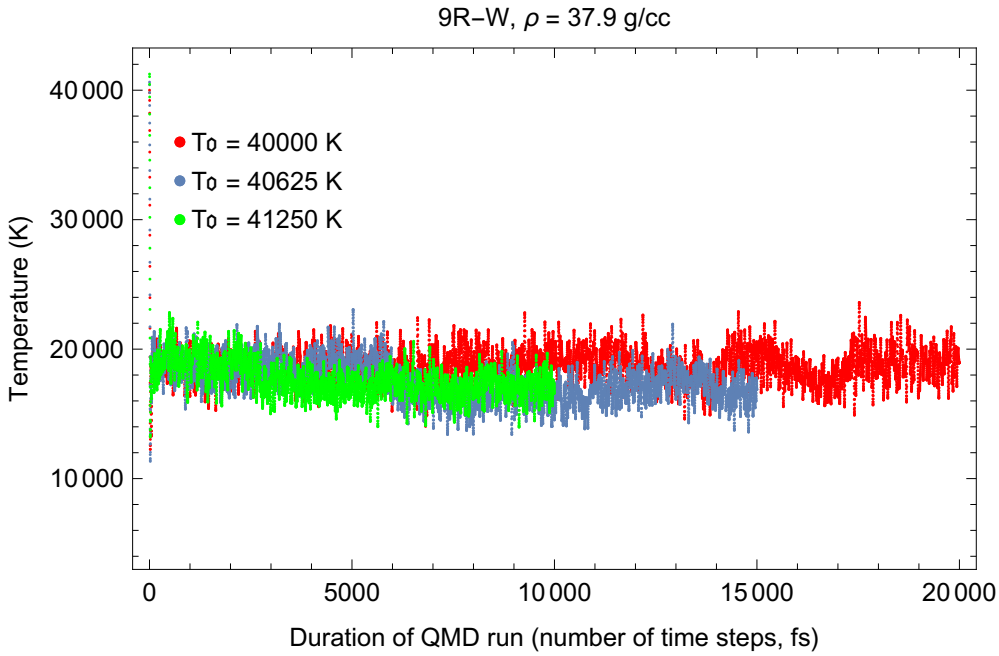

FIG. 11: The same as in Fig. 4 for 9R-W.

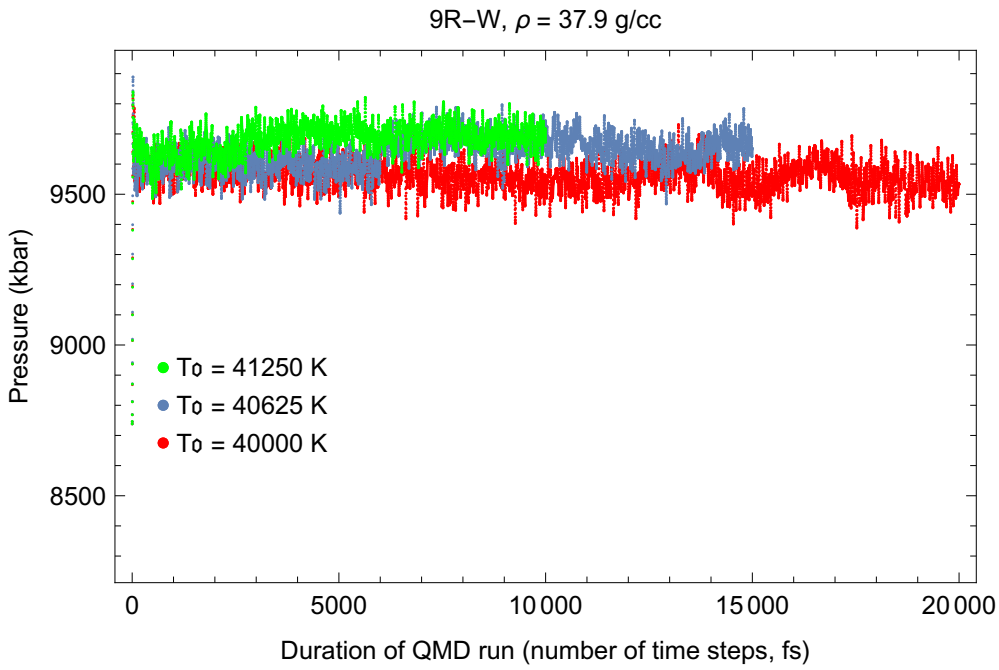

FIG. 12: The same as in Fig. 5 for 9R-W.

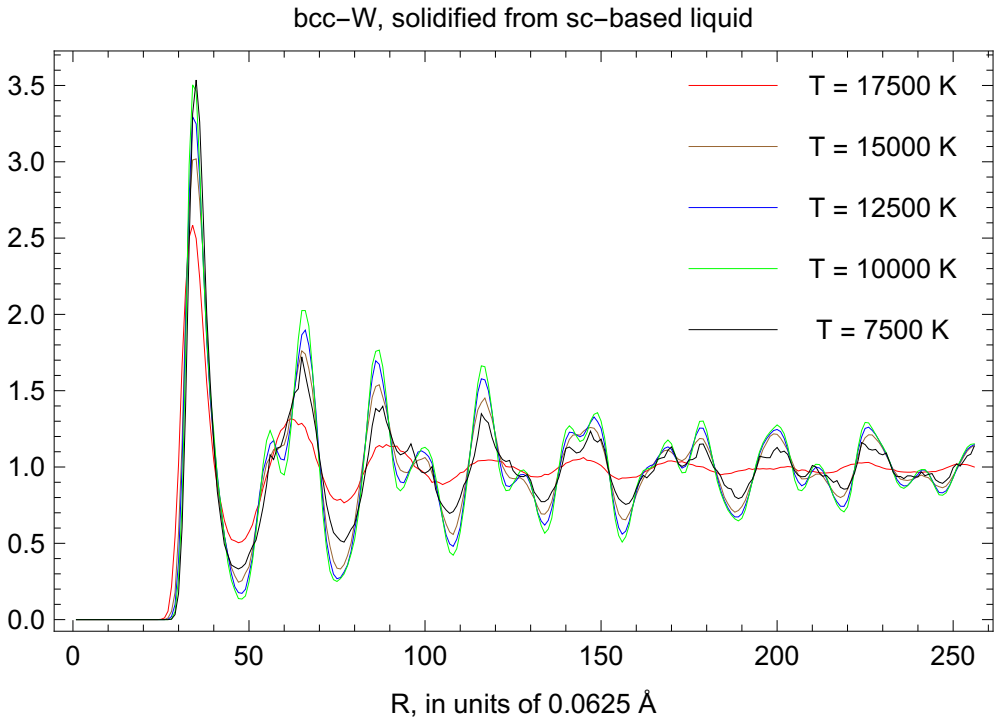

FIG. 13: RDFs of the final states of the solidification of liquid W at $\sim$ 1200 GPa at higher temperatures.

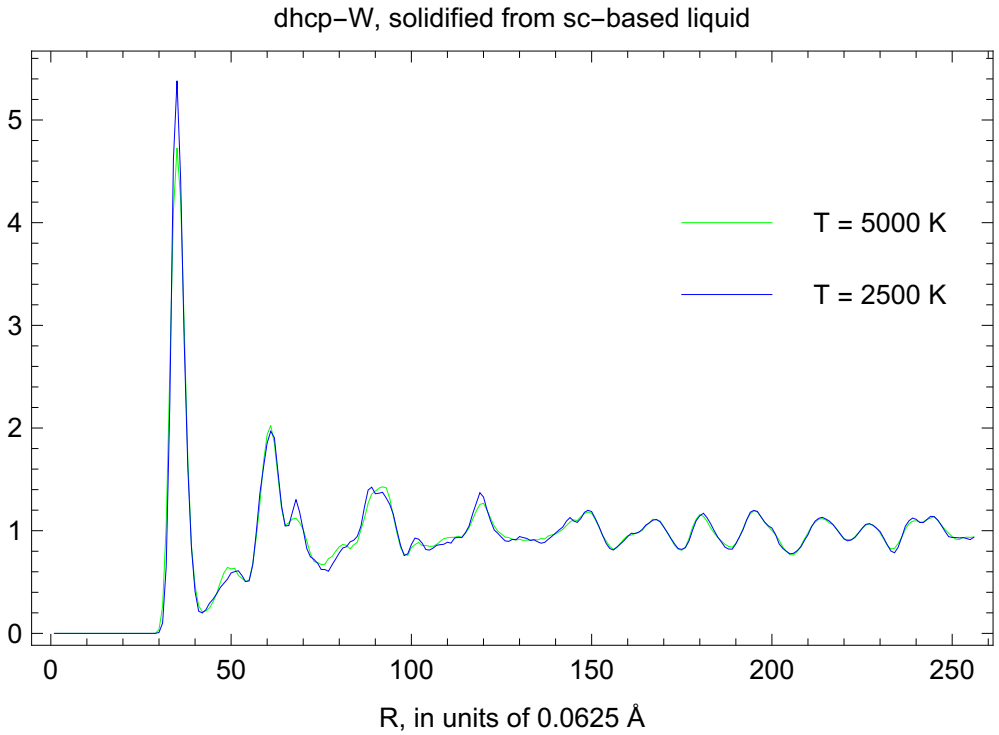

FIG. 14: RDFs of the final states of the solidification of liquid W at $\sim$ 1200 GPa at lower temperatures.